PAPER

Check for updates

Large magnetic entropy change and prediction of magnetoresistance using a magnetic field in La$_{0.5}$Sm$_{0.1}$Sr$_{0.4}$Mn$_{0.975}$In$_{0.025}$O$_3$

M. Dhahri, [ID] *[a] J. Dhahri [ID] [a] and E. K. Hlil[b]

A detailed study of the structural, magnetic, magnetocaloric and electrical effect properties in polycrystalline manganite La$_{0.5}$Sm$_{0.1}$Sr$_{0.4}$Mn$_{0.975}$In$_{0.025}$O$_3$ is presented. The X-ray diffraction pattern is consistent with a rhombohedral structure with $R\bar{3}c$ space group. Experimental results revealed that our compound prepared *via* a sol–gel method exhibits a continuous (second-order) ferromagnetic (FM) to paramagnetic (PM) phase transition around the Curie temperature (T_C = 300 K). In addition, the magnetic entropy change was found to reach 5.25 J kg^{-1} K^{-1} under an applied magnetic field of 5 T, corresponding to a relative cooling power (RCP) of 236 J kg^{-1}. We have fitted the experimental data of resistivity using a typical numerical method (Gauss function). The simulation values such as maximum resistivity (ρ_{max}) and metal–semiconductor transition temperature (T_{M-Sc}), calculated from this function, showed a perfect agreement with the experimental data. The shifts of these parameters as a function of magnetic field for our sample have been interpreted. The obtained values of β and γ, determined by analyzing the Arrott plots, are found to be T_C = 298.66 ± 0.64 K, β = 0.325 ± 0.001 and γ = 1.25 ± 0.01. The critical isotherm M (T_C, $\mu_0 H$) gives δ = 4.81 ± 0.01. These critical exponent values are found to be consistent and comparable to those predicted by the three-dimensional Ising model with short-range interaction. Thus, the Widom scaling law $\delta = 1 + \frac{\gamma}{\beta}$ is fulfilled.

1. Introduction

Over the past few years, magnetic refrigeration (MR) based on the magnetocaloric effect (MCE) has become a promising technology to replace the conventional gas-compression refrigeration due to its energy-efficient, environment-friendly advantages and economical benefits. It has been pointed out that suitable materials should be cost effective and possess a large MCE (large isothermal magnetic entropy change ΔS_M) over a wide temperature range. Among them, perovskite manganites with generic formula Ln$_{1-x}$A$_x$MnO$_3$ (Ln represents trivalent rare-earth elements such as La, Pr, Nd, Sm, *etc.*, and A stands for divalent alkaline-earth cations such as Ca^{2+}, Sr^{2+}, Ba^{2+}, *etc.*), have attracted considerable scientific and technological interest owing to their important magnetic and electrical properties,[1,2] such as the notable colossal magnetoresistance (CMR) and the magneto-caloric effect (MCE) under a moderate applied field, which is characterized by magnetic entropy change (ΔS_M) and relative cooling power (RCP). Furthermore, there is also a book written by Tishin and Spichkin[3] which describes numerous different magnetocaloric materials in detail.

Also, manganese oxides especially, the La–Sr based manganite (La$_{0.7}$Sr$_{0.3}$MnO$_3$) exhibit a metal–semiconductor transition (MSc) accompanied by a FM–PM transition near T_C. In a recent publication[4,5] there have been few models that can explain the transport mechanism in manganites. Among them, we point out the small polaron hopping (SPH) model and the 3D Mott's variable range hopping (VRH) in the semiconducting region, the adiabatic small polaron hopping mechanism[6] and electron–electron, electron–phonon processes in the metallic region. These laws are very important in manganite research because they very well describe the observed high-temperature variation ($T > T_{M-Sc}$) in the conduction mechanism.

However, there is still no clear conclusion of whether or not the resistivity $\rho(T)$ can be continuously predicted by temperature from the metal phase to the semiconductor phase for individual manganite with only one equation.

Unfortunately, few studies have been done on the mathematical model which can describe the carrier transport behavior of manganite as a function of temperature around the metal semiconducting transition and the relation between magnetic and electrical properties. In this contribution, we have determined the correlation between electrical and magnetic properties and we have developed a mathematical model to quantitatively analyze the temperature-dependent resistivity.

[a]Laboratoire de la matière condensée et des nanosciences, Univercité de Monastir, 5019, Tunisia. E-mail: mmay988205@gmail.com

[b]Institut Neel, CNRS et Univercité Joseph Fourrier, B. P. 166, 38042 Grenoble, France

Many previous reports were dedicated that the most accepted interpretations for the origin of these properties are the double exchange model and Jahn–Teller effect[7] which they are used to identify the magnetic phase transitions (FM–PM).

Therefore, to understand better the relation between CMR effect and the semiconductor–metal transition, two important questions about FM–PM transition should be clarified: one is the order of phase transition; the other is the common universality class. A most useful approach is the consideration of the critical exponents. These describing the thermodynamic properties near the phase transition can be used to elucidate interactions mechanisms near T_C. In earlier theoretical works,[8,9] the critical behavior related to the FM–PM transition in manganites within the DE model was first described with long-range mean-field theory. Later, depending on the computational technology for the CMR of manganites, Motome and Furukawa suggested that the FM–PM transition should belong to Heisenberg's universality Class.[10,11] However, some research have predicted that the critical exponents in manganites are in agreement with a short range exchange interaction model with the estimated critical exponent values related to either 3D-Heisenberg or 3D-Ising model.

Critical exponents for manganites show wide variation that almost covers all universality classes and different experimental tools are used for their determination. Ghosh et al.[12] reported that the calculated values of the critical exponent β is equal to 0.37 for the manganite $La_{0.7}Sr_{0.3}MnO_3$. However, $La_{0.8}Sr_{0.2}MnO_3$ is in good agreement with that in mean-field model[13] with a relative high value of β (=0.5). While a very low critical exponent of $\beta = 0.14$ identified in the single crystal $La_{0.7}Ca_{0.3}MnO_3$ suggested that the FM–PM transition in this system is of a first rather than second order type.[14] With this variety in mind, it is worthwhile to study the critical behavior in the same perovskite manganite.

The present work aims basically at investigating the structural, magnetic, magnetocaloric, electrical and the critical behavior for $La_{0.5}Sm_{0.1}Sr_{0.4}Mn_{0.975}In_{0.025}O_3$ (LSSMIO) manganite. We used four kinds of different theoretical models, which are mean field, 3D-Heisenberg, 3D-Ising, and tricritical mean field to explain the critical behavior in the manganite.

2. Experimental details

LSSMIO compound was fabricated using a conventional sol–gel method, it is known to produce very high quality, homogeneous and fine particle materials.

In this method, the stoichiometric amounts of high purity nitrate $Sr(NO_3)_2 \cdot 6H_2O$; $La(NO_3)_3 \cdot 6H_2O$; $Mn(NO_3)_2 \cdot 4H_2O$; $Sm(NO_3)_3 \cdot 6H_2O$ and $In(NO_3)_3 \cdot xH_2O$ precursors were taken as starting materials in appropriate stoichiometric ratio powder and pH was adjusted between 6.5 and 7. In the first step, the precursor solution was prepared by dissolving the constituents (precursors/starting materials) with desired composition in deionized water. In the next step, the homogeneous precursor solution was heated to 90 °C under constant stirring to eliminate the excess water and get a dry fluffy porous mass. Subsequently, the obtained sol was cooled before the addition of

ethylene glycol (EG) (1 : 1; EG : CA) and citric acid (CA) (CA : metal ion molar ratios of 1, 2 or 3) which they were used as polymerization/complexation (PC) agents. The process was heated first at 340–380 K with a vigorous stirring to evaporate water, accelerate the poly-esterification reaction between CA and EG and increase viscosity. Then the temperature was raised up to 450 K forming a dark viscous gel which slowly turned into a dark resin. This resin was easily powdered in an agate mortar and was calcined at 600 K for 7 h in oxygen atmosphere to eliminate the other organic compounds the carbons gases and give a fine powder. Finally, the resulting powder was uniaxial pressed at 105 Pa into pellets with a thickness of 2 mm and diameter of 8 mm. The obtained black pellets were sintered in air at 900 °C for 15 h.

Indeed, the microstructure was observed by a scanning electron microscope (SEM) using a Philips XL30 and semi-quantitative analysis was performed at a 20 kV accelerating voltage using energy dispersive X-ray analyses (EDAX). To extract the critical exponent of the sample accurately, the magnetic measurements were performed in the range of 0–5T, near the FM to PM phase transition using a BS1 and BS2 magnetometer developed in Louis Neel Laboratory, Grenoble. In fact, the isothermals are corrected by a demagnetization factor D_a that has been determined by a standard procedure from the low-field linear-response regime at a low temperature ($\mu_0 H_{appl} - D_a M$).

3. Results and discussion

3.1. Structural and morphological study

XRD patterns at room temperature (Fig. 1) confirmed that our sample have no trace of any impurity phase. The Bragg reflections indicate that our manganite crystallizes in a single phase with rhombohedral structure (space group $R\bar{3}c$). The structural parameters are refined by a standard Rietveld technique.[15] The refined XRD pattern for our sample is shown in Fig. 1 and the resulting lattice parameter as well as the corresponding
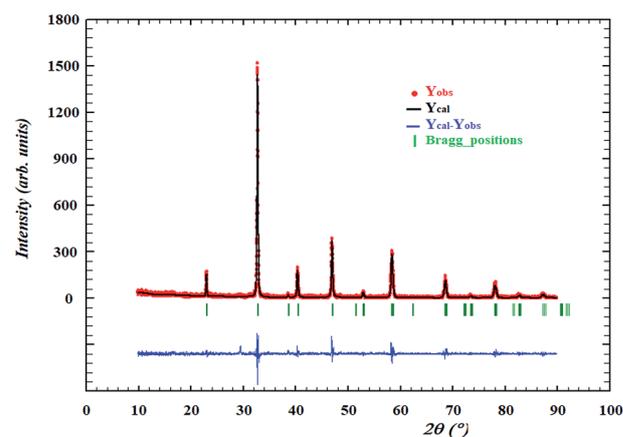

Fig. 1 Rietveld refinement for the sample LSSMIO. Experimental data (the point symbols), calculated data (the solid lines), difference between them is shown at the bottom of the diagram and Bragg positions are marked by vertical bars.

Table 1 Results of Rietveld refinements, determined from XRD patterns measured at room temperature for LSSMIO sample

Parameters	$La_{0.5}Sm_{0.1}Sr_{0.4}Mn_{0.975}In_{0.025}O_3$
Structure type	Rhombohedral
Space group	$R\bar{3}c$
Lattice parameter	
a (Å)	5.478(2)
c (Å)	13.379(5)
$V_{\text{unit cell}}$ (Å^3)	347.69
$(O)_{\text{Biso}}$ (Å^2)	1.530
$(O)_x$	0.4460(5)
$(La, Sm, Sr)_{\text{Biso}}$ (Å^2)	0.786(3)
$(Mn, In)_{\text{Biso}}$ (Å^2)	0.543(4)
Discrepancy factors (%)	
Bragg R-factor	2.14
R_{p}	6.7
R_{wp}	9.1
RF-factor	5.8
Goodness of fit χ^2	1.68

agreement factors are tabulated in Table 1. The substitution of In^{3+} for Mn^{3+} causes a distortion of cell, an elongation along the a and c axes, and as a result an increase of the cell volume.

The average crystallite size values have been estimated from the full width at half maximum of X-ray diffraction peaks and calculated using Scherer's equation given as:[16]

$$D_S = \frac{K\lambda}{\beta_{\text{Sch}}\cos\theta} \quad (1)$$

where K is the so-called shape factor, taking as 0.89, λ is the wave length of Cu Kα radiation ($\lambda = 1.54056$ Å), θ is Bragg's angle of the most intense peak and β_{Sch} is the line broadening at the full width at half maximum (FWHM) on the highest peak of plane (104), which is located at about $2\theta = 31°$ and defined as:

$$\beta_{\text{Sch}} = \beta_{\text{obs}}{}^2 - \beta_{\text{instr}}{}^2 \quad (2)$$

where, β_{obs} is the measured broadening and β_{instr} is the instrumental broadening of the diffraction peak from a standard silicon sample, defined by Caglioti's formula:[17]

$$(\beta^2)_{\text{instr}} = U\tan(\theta)^2 + V\tan(\theta) + W \quad (3)$$

Here U, V and W are scalars. The crystallite size, using eqn (1), is calculated from full width at half maximum (FWHM) of the peaks (104) (central peak).

The D_S value is found to be 87 nm. The SEM micrograph of our sample is shown in Fig. 2(b). Moreover, the average grain size was calculated using the average size linear intercept method from the micrograph. The value is $D_{\text{SEM}} = 210$ nm. We note that the grain size obtained by SEM (D_{SEM}) is much larger than that calculated by Scherrer's formula which can be explained by the fact that each particle observed by SEM is formed by several crystallized grains.[18]

In order to check the existence of all elements in these compounds, energy dispersive X-ray analysis (EDAX) was carried out at room temperature. EDAX spectrum represented in Fig. 2(a) reveals the presence of La, Sm, Sr, Mn, In and O elements, which confirms that there is no loss of any integrated elements during the sintering within experimental errors. The typical cationic composition for the sample is represented in Table 2. EDAX analysis shows that the chemical composition of the sample is close to the nominal one within the experimental uncertainties.

3.2. Magnetic and magnetocaloric study

Fig. 3 presents the temperature dependence of the magnetization measured in a constant magnetic field of $0.05T$ for LSSMIO sample. Apparently, our sample undergoes a phase transition from ferromagnetic (FM) to paramagnetic (PM) state at the ferromagnetic Curie temperature which is about $T_C = 300$ K, defined as the inflection point of dM/dT (inset. a Fig. 3). The phase transition of our sample is of second order. It also behaves a large of the range of temperature. This is a typical behavior of the sample fabricated by sol–gel method. The range of the wide of transition does not seems to reflect the chemical disorder but seems due to the disorder in magnetism. It may be

Table 2 Results of EDAX analysis of LSSMIO sample

Chemical species					
La	Sm	Sr	Mn	In	Nominal composition
0.499	0.101	0.389	0.974	0.026	$La_{0.5}Sm_{0.1}Sr_{0.4}Mn_{0.975}In_{0.025}O_3$
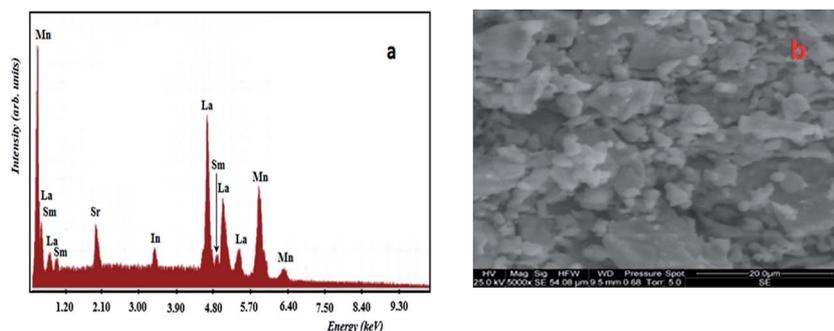
Fig. 2 (a) EDAX spectrum for LSSMIO compound. (b) Shows the typical SEM.
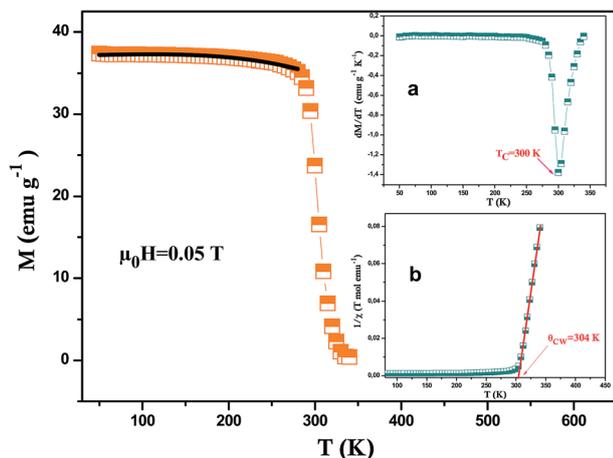
Fig. 3 Temperature dependence of magnetization $M(T)$ measured at 0.05T for LSSMIO sample and the solid line (black color) is the nonlinear curve fit following eqn (4). The (a) inset shows the plot of dM/dT as a function of temperature at $\mu_0 H = 0.05T$ and the (b)inset shows the temperature dependence of the inverse magnetic susceptibility.

in a result of phase separation phenomenal.[19] The experimental results showed that the doping of In^{3+} causes a substantial change in the magnetic properties of LSSMIO sample. Besides the ferromagnetism is due to the double exchange interaction between the Mn^{4+} and Mn^{3+} ions.[20] According to Lonzarich and Taillefer,[21] the manganites are ruled by spin wave theory. As for this theory magnetization varies as $T^{3/2}$ (Bloch's law) at very low temperatures[22] and as T^2 over a wide range of temperatures, whereas close to T_C, it varies as $(1 - T^{4/3}/T_C{}^{4/3})^{1/2}$. In view of this, the magnetization data in the ferromagnetic region have been fitted to an equation:

$$M(T) = M_0 + M_{3/2}T^{3/2} + M_2 T^2 \quad (4)$$

where M_0 is the temperature-independent spontaneous magnetization. The fitted curve is shown in Fig. 3. From the fitting, one may conclude that the ferromagnetic behavior of LSSMIO manganite type perovskite may be due to spin waves.

In order to better understand the magnetic behavior of our sample, we have fitted the inverse of the susceptibility as a function of temperature $\chi_0{}^{-1}(T)$ defined as $(M = \chi H)$ (inset. b Fig. 3), using the following Curie–Weiss (CW) law:

$$\chi = \frac{C}{T - \theta_{CW}} \quad (5)$$

where θ_{CW} is Curie–Weiss temperature, C is the Curie constant defined as:

$$C = \frac{N_A \mu_B{}^2}{3k_B}\mu_{eff}{}^2 \quad (6)$$

where $N_A = 6.023.1023$ mol^{-1} is Avogadro number; $\mu_B = 9.274 \times 10^{-21}$ emu is Bohr magneton and $k_B = 1.38016 \times 10^{-16}$ erg K^{-1} is Boltzmann constant.

Generally, the difference between ($\theta_{CW} = 304$ K) value and ($T_C = 300$ K) value depends on the substance and is associated with the presence of short-range ordered slightly above T_C,

which may be related to the presence of a magnetic inhomogeneity. From the determined Curie constant C, we have deduced the experimental effective moment μ_{eff}^{exp} using the following relation:[23]

$$\mu_{eff}^{exp} = \sqrt{3k_B C/N_A} = \sqrt{8C}\mu_B \quad (7)$$

where C is the inverse of the slope of the straight line. For Mn^{3+} or Mn^{4+}, the orbital moment is quenched ($L = 0$) so that S is the appropriate quantum number and we can write:

$$\mu_{eff}(S) = g\mu_B[S(S + 1)]^{1/2} \quad (8)$$

with $g = 2$ and $S = 3/2$ for (Mn^{4+}, 3d^3) or 2 (Mn^{3+}, 3d^4) which leads to $\mu_{eff} = 4.90\mu_B$ for Mn^{3+} and $\mu_{eff} = 3.78\mu_B$ for Mn^{4+}.

Then, we have calculated the effective paramagnetic moment per formula unit which can be written as:

$$\mu_{eff}^{theo} = \sqrt{(0.6 - x)\mu_{eff}{}^2(Mn^{3+}) + 0.4\mu_{eff}{}^2(Mn^{4+})} \quad (9)$$

The μ_{eff}^{exp} and μ_{eff}^{theo} values are 4.85 and 4.47, respectively. The experimental value of the effective paramagnetic moment is higher than the theoretical one. It is the signature of Mn^{4+} and Mn^{3+} clusters,[24] which can be explained by the presence of a short-range magnetic order in the paramagnetic phase. So that in this phase, the magnetic spins do not exist as individuals, they rather exist in small groups.

Magnetization *versus* magnetic field ($M - \mu_0 H$) curve of LSSMIO compound at 5 K is plotted in Inset. a Fig. 4. The sample closely reach a constant value of magnetization under an applied field $\mu_0 H = 1.5T$. The estimated magnetic moments from magnetization data at 5 K is $3.45\mu_B$ per formula unit. A rough estimation of the expected magnetic moment can be made, based on the chemical formula La$_{0.5}$$^{3+}Sm_{0.1}$$^{3+}Sr_{0.4}$$^{2+}$(Mn$_{0.6-x}$$^{3+}Mn_{0.4}$$^{4+}$)In$_x$$^{3+}O_3$$^{2-}$ leading to a magnetic moment: $M_{sp} = (4 \times (0.6 - x) + 3 \times 0.4)\mu_B = (3.6 - 4x)\mu_B$, as Mn^{3+} and Mn^{4+} ions have magnetic moments of $4\mu_B$ and $3\mu_B$ respectively.
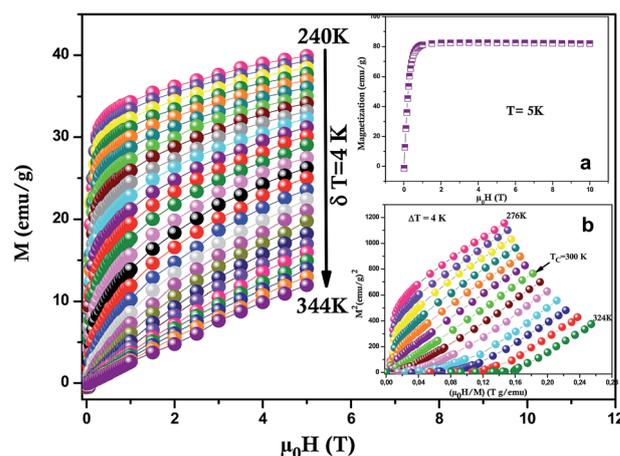

Fig. 4 Isothermal magnetization curves of LSSMIO sample. The (a) inset shows Magnetization *versus* field ($M - \mu_0 H$) curve at 5 K for LSSMIO sample. The (b) inset shows Standard Arrott plot (isotherms M^2 vs. $\mu_0 H/M$).

The calculated value of magnetic moment per formula unit is $3.5\mu_B$ for our sample.

The magnetocaloric effect MCE which is an intrinsic property of all magnetic materials, is the tendency of the material to heat up or cool down during the application or removal of a magnetic field. The applied importance of the MCE is easily appreciated from the fact that for many years it has been used successfully to reach ultra-low temperatures in a research environment.[25,26] Besides, it is maximized when the material is near its magnetic ordering temperature (Curie temperature T_C). In order to examine this property we have carried out the isothermal $M(\mu_0 H)$ measurements at different temperatures (with temperature interval $\delta T = 4$ K) in the FM–PM transition region for the sample (Fig. 4). To guarantee that magnetization data were determined in isothermal conditions, the sweep rat of the magnetic field was set slowly enough. The magnetization curve of LSSMIO manganite at temperatures below T_C exhibit sharp increase of magnetization at low fields and then a gradual saturation at high fields reflecting a paramagnetic behavior.[27] This magnetization is all the smaller as the temperature is high, which means that the thermal agitation is important.

In order to enquire the efficiency of our sample in the magnetic refrigeration systems, the magnetic entropy change $\Delta S_M(T, \mu_0 H)$ due to the application of a magnetic field $\mu_0 H$ can be calculated from a family of isothermal M–$\mu_0 H$ curves, using the following formula:

$$\Delta S_M(T, \ \mu_0 H) = S_M(T, \ \mu_0 H) - S_M(T, \ 0)$$
$$= \int_0^{\mu_0 H_{max}} \left(\frac{\partial S}{\partial(\mu_0 H)} \right)_{\mu_0 H} \mu_0 dH \qquad (10)$$

From Maxwell relation $(-\Delta S_M)$ was induced by changing the magnetic field from zero to $(\mu_0 H)$:

$$\left(\frac{\partial M}{\partial T} \right)_{\mu_0 H} = \left(\frac{\partial S}{\partial(\mu_0 H)} \right)_T \qquad (11)$$

where $\left(\frac{\partial M}{\partial T} \right)_{\mu_0 H}$ is the experimental value obtained from $M(T)$ curves under magnetic field $\mu_0 H$. One can use the following expression:

$$\Delta S_M \left(\frac{T_1 + T_2}{2} \right) = \left(\frac{1}{T_1 - T_2} \right) \left[\int_0^{\mu_0 H_{max}} M(T_2, \ \mu_0 H)\mu_0 dH \right.$$
$$\left. - \int_0^{\mu_0 H_{max}} M(T_1, \ \mu_0 H)\mu_0 dH \right] \qquad (12)$$

Using eqn (12), we have calculated the magnetic entropy change under different field changes for LSSMIO manganite as seen in Fig. 5. The change of magnetic entropy of a magnetic material has the largest value near a phase transition, where the magnetization changes rapidly with temperature.[28,29]

The peak magnitude increases with the increase in the applied magnetic field $\mu_0 H$ but the peak position is closely unaffected because of the second order nature of the ferromagnetic transition in this compound. It should be noted that for each magnetic applied field $(-\Delta S_M^{max})$ reaches the maxima
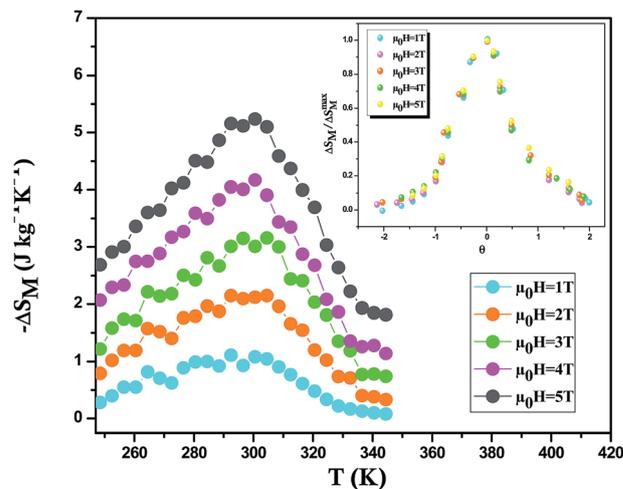

Fig. 5 Temperature dependence of magnetic entropy change under different external fields for LSSMIO compound. The inset shows universal behavior of the scaled entropy change curves of LSSMIO sample at different fields.

value at the Curie temperature ($T_C = 300$ K). The values of $(-\Delta S_M^{max})$, which increases with increasing the applied magnetic field, are 5.25 and 2.11 kg^{-1} K^{-1} upon a magnetic field change of $5T$ and $2T$, respectively.

On the other hand, magnetic refrigerants are desired to have not only a large $(-\Delta S_M)$ but also a large refrigerant relative cooling power (RCP). This factor corresponds to the amount of heat per kilogram that can be transferred between the cold and hot tanks during an ideal refrigeration cycle and defined as:[30]

$$RCP = -\Delta S_M^{max} \times \delta T_{FWHM} \qquad (13)$$

where ΔS_M^{max} is the maximum magnetic entropy change and $\delta T_{FWHM} = T_{hot} - T_{cold}$ is the temperature difference at the full width at half maximum of the magnetic entropy change curve.

The RCP values as well as the maximum values of the magnetic entropy change under a magnetic applied field of $5T$ are summarized in Table 3. We remarque that the RCP factor undergo a moderate increase with the amplification of the magnetic field. The significant value of the RCP would confirms the transport of a greater amount of heat in an ideal refrigeration cycle. We can see that these results are interesting compared with other compounds[31–38] reported in the literature (Table 3), so we can estimate that our compound is a potential candidate to be used in the magnetic refrigeration.

Franco et al.[39] proposed that the phenomenological universal curve is made by normalizing all the magnetic entropy change $(\Delta S(T, \mu_0 H)/\Delta S_M^{max})$. Here, ΔS_M^{max} presents the peak maximum of the magnetic entropy change at different magnetic fields (shown in Inset. Fig. 5) and by rescaling the temperature axis, namely (θ), below and above T_C, as noted:

$$\theta = \begin{cases} (T_C - T)/(T_{r_1} - T), & T \leq T_C \\ (T - T_C)/(T_{r_2} - T_C), & T \geq T_C \end{cases} \qquad (14)$$

Knowing that T_{r_1} and T_{r_2} present the temperatures of two reference points corresponding to $\Delta S_M(T_{r_{1,2}}) = 1/2\Delta S_M^{max}$. It's

Table 3 Maximum entropy change ΔS_M^{max} and relative cooling power (RCP), for $La_{0.5}Sm_{0.1}Sr_{0.4}Mn_{0.975}In_{0.025}O_3$, occurring at the Curie temperature (T_C) and under magnetic field variations, $\Delta H = 5T$, compared to several materials considered for magnetic refrigeration

Material	T_C (K)	μ_0H (T)	ΔS_M^{max} (J kg^{-1} K^{-1})	RCP (J kg^{-1})	Ref.
$La_{0.5}Sm_{0.1}Sr_{0.4}Mn_{0.975}In_{0.025}O_3$	300	5	5.25	236	This work
Gd	293	5	9.5	410	31
$Gd_5Si_2Ge_2$	275	5	18.5	535	32
$La_{0.7}Sr_{0.3}MnO_3$	370	5	5.15	252	33
$La_{0.7}Ca_{0.3}MnO_3$	264	5	7.7	—	34
$La_{0.7}Ca_{0.2}Sr_{0.1}MnO_3$	308	5	7.5	374	35
$La_{0.57}Y_{0.1}Ba_{0.23}Ca_{0.1}MnO_3$	300	5	4.34	349	36
$La_{0.67}Sr_{0.33}Mn_{0.9}Cr_{0.1}O_3$	328	5	5	—	37
$La_{0.7}Ca_{0.1}Pb_{0.2}Mn_{0.9}Al_{0.05}Sn_{0.05}O_3$	295	5	2.3	135	38
$La_{0.7}Ca_{0.1}Pb_{0.2}Mn_{0.85}Al_{0.075}Sn_{0.075}O_3$	290	5	2	176	38

clear from this figure that the experimental points distribute on one universal curve. The existence of the universal curve of $(-\Delta S_M)$ around T_C confirms the second nature order phase transition.

3.3. Prediction of electrical resistivity

Fig. 6 shows the resistivity *versus* temperature behavior of LSSMIO manganite at an applied magnetic field of 0 to 5T. Our sample exhibit metal–semiconducting transition at a temperature $T_{M–Sc}$ which is obtained from the inflection point of dρ/dT plots. The resistivity of manganite is determined by several parameters such as the applied magnetic field, temperature, composition and so on. To understand these properties of the sample, based on the mathematical relationship between the resistivity and magnetic field or the temperature, we have to fit these curves. Shi[40] reported that there are two paths for curve fitting: One way is to directly apply the fitting function; another way is to create a mathematical model when there is no

appropriate fitting function available. According to this suggestion and after checking the fitting function, we can say that the Gauss function, which is a typical numerical method with a nonlinear curve fitting for the quantitative analysis, offers such an opportunity. The applicable Gauss function is expressed by:

$$\rho(T) = \rho(T_u) + \frac{A}{w\sqrt{\pi/2}}\exp\left(-2(T - T_d)^2 / w^2\right) \quad (15)$$

where $\rho(T_u)$, A, T_d, and w are constants obtained from the fitting process.

If the Gauss function (14) is available for predicting resistivity at temperatures across the measurement range for our compound, the minimum value of ρ is given by $\rho(T|_{T\to\infty})$. Thus, the physical significance of parameter $\rho(T_u)$ is the resistivity of manganite materials at high temperatures. The maximum value of ρ is given by the parameters $\rho(T_u)$, A, and w in the following form:
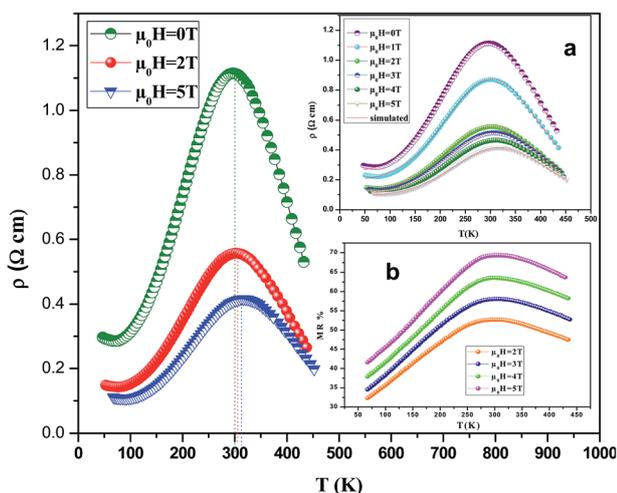
$$\rho_{max} = \rho|_{T\to\infty} + \frac{A}{w\sqrt{\pi/2}} \quad (16)$$

So, the Gauss function (14) will be rewrite as:

$$\rho(T) = \rho_{min} + \frac{A}{w\sqrt{\pi/2}}\exp\left(-2(T - T_d)^2 / w^2\right) \quad (17)$$

We analyses the resistivity curves of LSSMIO compound at different magnetic field using the above approach (17). Optimized parameters employed to simulate the component spectra are also listed in Table 4 and the fitted curves are shown in Inset. a Fig. 6.

The correlation coefficient R^2 (Table 4) which is close to 1, showed a satisfactory agreement between experimental and the modeled data which implies that the metal–insulator transition temperature, $T_{M–Sc}$ can be confirmed more precisely by the Gauss function simulation for our compound. The comparison between the peaks of the best-fitted value of T_d, determined from Gauss function, and the experimental data demonstrated that parameter T_d corresponds to the metal–semiconducting transition temperature, $T_{M–Sc}$.

Fig. 6 Resistivity *vs.* temperature curves of LSSMIO sample under different applied magnetic fields rising from 0 to 5T. The (a) inset shows experimental (symbol) and estimated (line) electrical resistivity as a function of temperature of LSSMIO sample under different applied magnetic field. The (b)inset shows the variation of MR *vs. T* curves for LSSMIO sample under applied magnetic field of 2, 3, 4 and 5T.

Table 4 The obtained constants determined fitting the experimental data using eqn (17)

	Calculated Gauss function	R^2
$La_{0.5}Sm_{0.1}Sr_{0.4}Mn_{0.975}In_{0.025}O_3$ $0T$	$\rho(T) = 0.247 + \dfrac{196.710}{160.145\sqrt{\pi/2}} \exp(-2(T - T298.236)^2/160.145^2)$	0.997
$La_{0.5}Sm_{0.1}Sr_{0.4}Mn_{0.975}In_{0.025}O_3$ $1T$	$\rho(T) = 0.193 + \dfrac{153.679}{165.324\sqrt{\pi/2}} \exp(-2(T - 301.636)^2/165.324^2)$	0.989
$La_{0.5}Sm_{0.1}Sr_{0.4}Mn_{0.975}In_{0.025}O_3$ $2T$	$\rho(T) = 0.123 + \dfrac{98.355}{168.544\sqrt{\pi/2}} \exp(-2(T - 303.836)^2/168.544^2)$	0.998
$La_{0.5}Sm_{0.1}Sr_{0.4}Mn_{0.975}In_{0.025}O_3$ $3T$	$\rho(T) = 0.114 + \dfrac{91.069}{173.140\sqrt{\pi/2}} \exp(-2(T - 308.376)^2/173.140^2)$	0.996
$La_{0.5}Sm_{0.1}Sr_{0.4}Mn_{0.975}In_{0.025}O_3$ $4T$	$\rho(T) = 0.103 + \dfrac{82.305}{177.369\sqrt{\pi/2}} \exp(-2(T - 311.936)^2/177.369^2)$	0.987
$La_{0.5}Sm_{0.1}Sr_{0.4}Mn_{0.975}In_{0.025}O_3$ $5T$	$\rho(T) = 0.092 + \dfrac{73.399}{180.412\sqrt{\pi/2}} \exp(-2(T - 318.236)^2/180.412^2)$	0.995

Thus, the transition temperature T_{M-Sc} can be confirmed more precisely for other magnetic fields using the appropriate Gauss function simulation.

The Fig. 7 illustrates the dependency of ρ_{max} on the applied magnetic field for LSSMIO sample. The best fit of this curve show that the successful logistics equation could properly give a quantitative relationship between ρ_{max} and magnetic field μ_0H via nonlinear curve fitting, and the logistic function is given by:

$$\rho_{max}(\mu_0H) = A + \frac{A - B}{1 + \left(\dfrac{\mu_0H}{C}\right)^P} \qquad (18)$$

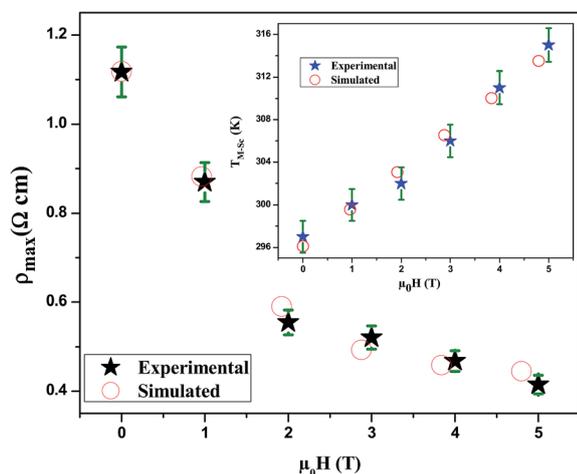The optimized parameters A, B, C and P will be determined from the fitting of the experimental data (Table 5).

Fig. 7 Experimental and simulated ρ_{max} as a function of magnetic field. The inset shows T_{M-Sc} vs. μ_0H for LSSMIO compound.

The plots of ρ_{max} versus magnetic field for LSSMIO compound have been fitted with the logistic model, which successfully describes the experimental behavior of the maximum resistivity ρ_{max} of our sample. According to this model, it's clear that ρ_{max} decreases with an increased magnetic field μ_0H, which implies a logistic increase in the carrier density. For this reason, it is appropriate to use the logistic model for predicting the maximum resistivity ρ_{max} before one magnetic field is applied.

It's clear from Fig. 6 that T_{M-Sc} shifts toward higher temperatures when μ_0H increases, which confirm that there is a relationship between T_{M-Sc} and the applied magnetic field. Inset. Fig. 7 shows the construct of the T_{M-Sc} of LSSMIO compound as a function of applied magnetic field. We can see that there is a linear relationship between the two variables.

Therefore, the functional form between T_{M-Sc} and magnetic field is expressed by a line eqn (19), and it is given by:

$$T_{M-Sc}(\mu_0H) = S \times \mu_0H + I \qquad (19)$$

The obtained constants are illustrated in Table 5. Notably, it can be observed that the theoretical results of T_{M-Sc} derived by eqn (19) are consistent with the experimental data in Table 4. Therefore, it may be stated that the magnetic field is correlative with T_{M-Sc}. In addition, it is appropriate to use eqn (19) in forecasting T_{M-Sc} before one magnetic field is applied.

The shifts of the T_{M-Sc} to the high-temperature range with the increase of the applied magnetic field can be explained by the reduction in the charge carriers delocalization uniformly caused by the applied magnetic field, which in turn might result in reducing the resistivity and also cause local ordering of the magnetic spins in the same way. Due to this linear ordering, the FM metallic state may suppress the PM insulating regime. Therefore, it may be stated that the conduction electrons (eg^1)

Table 5 The obtained constants determined fitting the experimental data using eqn (18) and (19)

	A	B	C	P	S	I
$La_{0.5}Sm_{0.1}Sr_{0.4}Mn_{0.975}In_{0.025}O_3$	0.426	−0.265	1.231	2.632	3.628	296.095

are completely polarized inside the magnetic domains hence, the peak temperature (T_{M-Sc}) shifts to the high temperature side with applications of the magnetic field.

3.4. Study of magnetoresistance

The magnetoresistance MR is a fundamental property of manganites, which is related to the reduction of the electrical resistivity of the material by applying a magnetic field, it is given by:

$$\text{MR}(\%) = \frac{\Delta\rho}{\rho} = \frac{\rho(H=0) - \rho(H)}{\rho(H=0)} \times 100 \qquad (20)$$

where $\rho(H=0)$ is resistivity under a zero magnetic field and $\rho(H)$ is resistivity under different applied fields.

Inset b Fig. 6 presents the variation of MR as a function of the temperature at different applied magnetic fields (2–5T). It is very interesting to note from this figure that MR presents a pic around T_C then it gradually decreases at high temperatures. The maximum magnetoresistance values of our compound at the metal–semiconducting (MSc) transition temperature are found 52%, 58%, 63% and 69% under applied magnetic field of 2, 3, 4 and 5T, respectively.

The reason for the higher MR% observed at high temperature is attributed to the involved spin polarized tunneling between grains or spin dependent scattering of polarized electron at grain boundaries.[41,42]

3.5. Critical behavior

For a continuous phase transition around the critical temperature, its thermodynamic function can be expressed by a power law form with three critical exponents. We would like to make a brief mention of the definitions of these exponents, namely β (associated with the spontaneous magnetization M_S), γ (associated with initial susceptibility χ_0^{-1}) and δ (associated with the critical magnetization isotherm (magnetization M versus magnetic field $\mu_0 H$ at T_C).[8,43] The mathematical definitions of the exponents from magnetization measurements are given in the following relations:

$$M_s(T) = M_0 |\varepsilon|^{-\beta}, \varepsilon < 0, T < T_C \qquad (21)$$

$$\chi_0^{-1}(T) = (h_0/M_0)\varepsilon^{\gamma}, \varepsilon > 0, T > T_C \qquad (22)$$

$$M = DH^{1/\delta}, \varepsilon = 0, T = T_C \qquad (23)$$

Here ε is the reduced temperature ($\varepsilon = (T - T_C)/T_C$); h_0 as well as M_0 and D are the critical amplitudes.

In our work, we have used different methods to investigate the critical behavior of the LSSMIO sample, namely the modified Arrott plots (MAP) method, the Kouvel–Fisher method (KF) and critical isotherm analysis (CI).[44,45] The first method used to calculate the critical exponents is the MAP method (also called Arrott–Noakes plots). In this technique, the $M = f(\mu_0 H)$ data is converted into series of isothermal ($M^{1/\beta}$ vs. $(\mu_0 H/M)^{1/\gamma}$) depending on the following relation:[44]

$$(\mu_0 H/M)^{1/\gamma} = (T - T_C)/T_1 + (M/M_1)^{1/\beta} \qquad (24)$$

where β and γ are the critical exponents and M_1 is a material constant. Inset b Fig. 4 shows the Arrott plot M^2 vs. $\mu_0 H/M$ constructed from the raw M–$\mu_0 H$ isotherms after correcting the external magnetic field for demagnetization effects. The advantages of this plot are that T_C can be determined accurately, since the isotherm at T_C will pass through the origin; it directly gives $\chi_0^{-1}(T)$ as an intercept on $\mu_0 H/M$ axis and intercept on positive M^2 axis gives $M_S(T)$. One can see that all the curves in this plot show nonlinear behavior having downward curvature even in high field indicating non-mean-field-like behavior. Moreover, the concave downward curvature clearly indicates second-order phase transition according to the criterion suggested by Banerjee.[46]

Fig. 8(a–c) shows the modified Arrott plots (MAP) based on the Arrott–Noakes equation of state eqn (24), at different temperatures by using the 3D Ising model ($\beta = 0.325$, $\gamma = 1.240$), the 3D Heisenberg model ($\beta = 0.365$, $\gamma = 1.336$) and the tricritical mean field ($\beta = 0.25$, $\gamma = 1$), respectively for LSSMIO compound. In order to select the best model which describes this system, we calculated their relative slopes (RS) which are defined as: $RS = S(T)/S(T_C)$ (where $S(T)$ is the slope of the quasi-straight line in the high-field region at T). In the most ideal case, all RSs should be equal to 1 because the modified Arrott plot is a series of parallel straight lines.

Fig. 8(d) shows the RS vs. T curve for LSSMIO sample for the four models, mean field model, 3D-Heisenberg, 3D-Ising and tricritical mean field model. The RS of 3D-Heisenberg and tricritical mean-field models obviously deviates from the straight line of RS = 1 but the RS of 3D-Ising model is around to this line. Therefore, the first Arrott plot gives the best results among these three models, indicating the critical properties of LSSMIO compound can be described with 3D-Ising model.

Based on these isotherms, the spontaneous magnetization $M_S(T, 0)$ and the inverse susceptibility $\chi_0^{-1}(T)$ data are extracted from the linear extrapolation from the high-field region to the intercepts with the axes $M^{1/\beta}$ and $(\mu_0 H)^{1/\gamma}$, respectively. In Fig. 9(a) we have plotted the temperature dependence of $M_S(T, 0)$ as green squares and $\chi_0^{-1}(T)$ as blue squares with their fitting curves using eqn (21) and (22), respectively. We find that the final fitted curves reproduce the experimental data perfectly and give two sets of critical exponents (Table 6). It can be seen that T_C obtained from the critical analysis of the modified plot agrees well with that obtained from the $M(T)$ curves in Fig. 3, and the obtained critical exponents are very close to those in the 3D Ising model.

As the next step in the scaling analysis, we have followed the Kouvel Fisher method to determine more accurately β, γ and T_C.[47]

$$M_S(T)[dM_S(T)/dT]^{-1} = (T - T_C)/\beta \qquad (25)$$

$$\chi_0^{-1}(T)[d\chi_0^{-1}(T)/dT]^{-1} = (T - T_C)/\gamma \qquad (26)$$

After this method both $M_S[dM_S/dT]^{-1}$ and $\chi_0^{-1}[d\chi_0^{-1}/dT]^{-1}$ have a linear behavior with respect to T with slopes $1/\beta$ and $1/\gamma$, respectively, as shown in Fig. 9(b).

One of the advantages of this method is that the value of the critical temperature is not introduced a priori but extracted
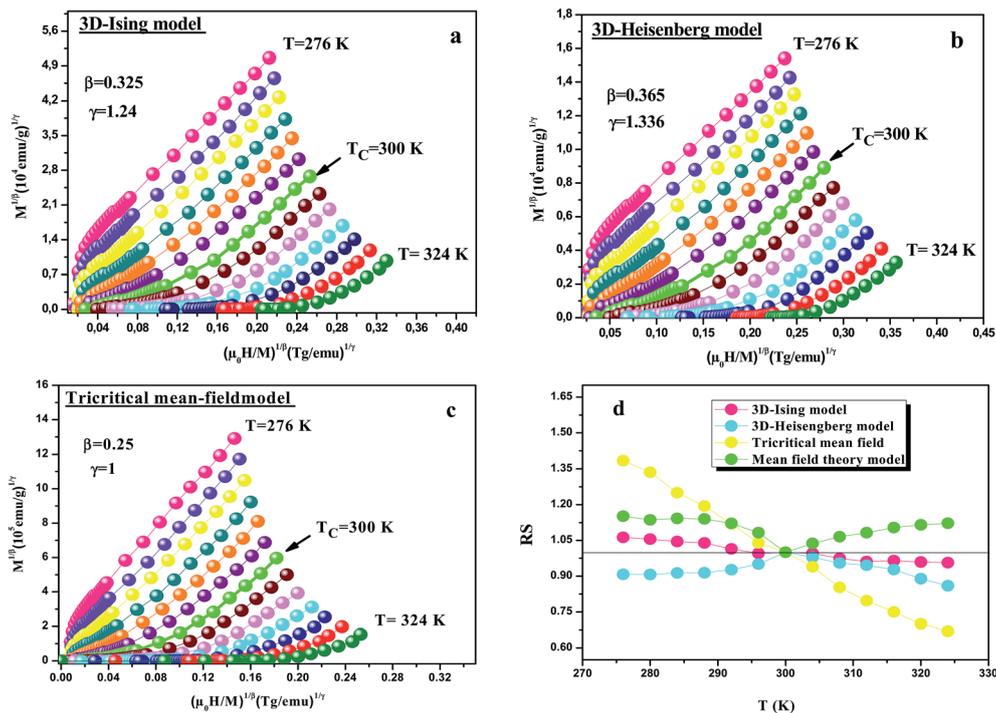
Fig. 8 Modified Arrott plot isotherms of $M^{1/\beta}$ vs. $(\mu_0 H/M)^{1/\gamma}$ for LSSMIO sample, with (a) 3D Ising-model ($\beta = 0.325$ and $\gamma = 1.24$); (b) 3D Heisenberg model ($\beta = 0.365$ and $\gamma = 1.336$); (c) tricritical mean-field model ($\beta = 0.25$ and $\gamma = 1$) and (d) shows the relative slope (RS) as a function of temperature using several methods.
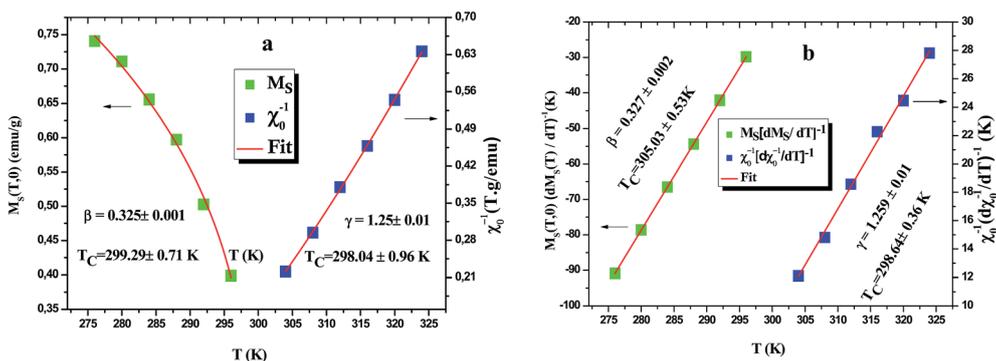

Fig. 9 (a) Temperature dependences of the spontaneous magnetization $M_S(T)$ (left) and inverse initial susceptibility $\chi_0^{-1}(T)$ (right) for LSSMIO sample. (b) Kouvel–Fisher plots of $M_S(T)[dM_S(T)/dT]^{-1}$ (left) and $\chi_0^{-1}(T)[d\chi_0^{-1}(T)/dT]^{-1}$ vs. T (right) of LSSMIO sample.

from the intercept of the straight fitted lines on the temperature axis. The values of β, γ and T_C obtained by KF method are also summarized in Table 6.

It is worth remarking how MAPs and the Kouvel Fisher method give close values of all critical parameters, confirming the robustness of the results. After eqn (23), the critical exponent δ can be extracted from the fitting of the critical isotherm to be compared with the values obtained from the scaling law (eqn (27)). Inset Fig. 10 shows the critical isotherm at $T = 300$ K in log–log scale as this should render a straight line (as it happens), whose slope is δ. We obtained $\delta = 4.81 \pm 0.01$ for LSSMIO compound (Table 6).

Furthermore, according to the statistical theory, these three critical exponents have to obey the Widom scaling relation:[48]

$$\delta = 1 + \frac{\gamma}{\beta} \qquad (27)$$

Using this scaling relation, the value of δ is equal to 4.84 for β and γ obtained from the MAP method. Thus, the critical exponents found in this study obey the Widom scaling relation remarkably well, implying that the obtained β and γ values are reliable.

To put our obtained results in the context of previous works, we summarize in the Table 6 the values of the critical exponents obtained for our sample, those expected from theoretical models[49,50] and the previous reports on Sr-doped manganites. It is found that the value of ($\beta = 0.325 \pm 0.001$) for our compound

Table 6 Comparison of the critical exponents of LSSMIO with those from the various theoretical models and with earlier reports (MAP: modified Arrott plot, KF: Kouvel–Fisher method, δ cal: the δ values calculated directly according to the Widom scaling relationship $\delta = 1 + \frac{\gamma}{\beta}$, δ exp: the δ values obtained by critical isotherm (CI) fitting)

| Material	Method	T_C (K)	β	γ	δ	Ref.
Mean-field model	Theory		0.5	1.0	3.0	49
3D-Heisenberg model	Theory		0.365 ± 0.003	1.336 ± 0.004	4.80 ± 0.04	49
3D-Ising model	Theory		0.325 ± 0.002	1.241 ± 0.002	4.82 ± 0.02	49
Tricritical mean-field model	Theory		0.25	1	5	50
$La_{0.5}Sm_{0.1}Sr_{0.4}Mn_{0.975}In_{0.025}O_3$	MAP	298.66 ± 0.64	0.325 ± 0.001	1.25 ± 0.01		This work
	KF	301.83 ± 0.43	0.327 ± 0.002	1.259 ± 0.001		This work
	CI (cal)	—	—	—	4.84	This work
	CI (exp)	—	—	—	4.81 ± 0.01	
$La_{0.7}Ca_{0.2}Sr_{0.1}Mn_{0.85}Cr_{0.15}O_3$		234.54 ± 0.6	0.322 ± 0.03	1.2 ± 0.17	4.752	51
$La_{0.6}Sr_{0.4}Mn_{0.9}V_{0.1}O_3$		356.407	0.316	1.243	4.947	52
$La_{0.6}Ca_{0.2}Sr_{0.2}MnO_3$		344.456	0.498	1.053	2.992	53
$La_{0.57}Nd_{0.1}Sr_{0.33}MnO_3$		352.23	0.368	1.191	4.236	54
$La_{0.7}Ca_{0.2}Sr_{0.1}MnO_3$		284	0.394	0.925	3.34	55
$La_{0.75}Sr_{0.25}MnO_3$		—	0.40 ± 0.02	1.27 ± 0.06	4.12 ± 0.33	56
$La_{0.7}Sr_{0.3}MnO_3$		360.2	0.377 ± 0.004	1.168 ± 0.006	4.10 ± 0.01	57
$La_{0.7}Sr_{0.3}Mn_{0.95}Co_{0.05}O_3$		320.4	0.403 ± 0.005	1.159 ± 0.007	3.88 ± 0.01	57
$La_{0.7}Sr_{0.3}Mn_{0.9}Co_{0.1}O_3$		281.6	0.457 ± 0.007	1.114 ± 0.005	3.44 ± 0.01	57
$La_{0.7}Sr_{0.3}Mn_{0.85}Co_{0.15}O_3$		273.9	0.418 ± 0.004	1.187 ± 0.006	3.84 ± 0.01	57
$La_{0.5}Sm_{0.1}Sr_{0.4}MnO_3$		313.36 ± 0.36	0.324 ± 0.01	1.240 ± 0.13	4.83 ± 0.01	58

is quite close to that expected from 3D Ising model ($\beta = 0.325 \pm 0.002$). Similar results have been found for other compounds such as $La_{0.7}Ca_{0.2}Sr_{0.1}Mn_{0.85}Cr_{0.15}O_3$ (ref. 51) and $La_{0.6}Sr_{0.4}Mn_{0.9}V_{0.1}O_3$ (ref. 52) with $\beta = 0.322 \pm 0.03$ and $\beta = 0.316$, repectively. However, few other Sr-doped compounds, listed in Table 6, have β values close to those of the mean field and 3D Heisenberg models, such as $La_{0.6}Ca_{0.2}Sr_{0.2}MnO_3$ with ($\beta = 0.498$ and $\gamma = 1.053$),[53] $La_{0.57}Nd_{0.1}Sr_{0.33}MnO_3$ with ($\beta = 0.368$ and $\gamma = 1.191$)[54] and $La_{0.7}Ca_{0.2}Sr_{0.1}MnO_3$ with ($\beta = 0.394$ and $\gamma = 0.925$).[55] Besides, the critical exponent values of $La_{0.75}Sr_{0.25}MnO_3$ compound[56] are all between mean-field values and three-dimensional-(3D)-Ising-model values ($\beta = 0.40 \pm 0.02$, $\gamma = 1.27 \pm 0.06$), but those determined for $La_{0.7}Sr_{0.3}Mn_{1-x}Co_xO_3$ sample[57] do not belong to any universality class ($\beta = 0.403 \pm$

0.005; $\gamma = 1.159 \pm 0.007$ for $x = 0.05$) and ($\beta = 0.457 \pm 0.007$; $\gamma = 1.114 \pm 0.005$ for $x = 0.1$). To further understand the magnetic interactions in In-doped perovskite manganite, in earlier studies we have carefully investigated the critical behavior of the reference compound $La_{0.5}Sm_{0.1}Sr_{0.4}MnO_3$ (ref. 58) ($\beta = 0.324 \pm 0.01$; $\gamma = 1.240 \pm 0.13$). It belong to the same universality class (3D Ising model) and it show that short-range ferromagnetic order is present in the reference compound around the critical temperature.

Performing a renormalization group analysis of exchange interaction systems, Fisher *et al.*[59] have found that the values of the critical parameters depend on the range of exchange interactions with the form $J(r) = 1/r^{d+\sigma}$ (d and σ are the dimension of the system and the interaction range, respectively). It has been argued that, if σ is greater than 2, the Heisenberg framework is valid for a 3D-isotropic ferromagnet, However, if σ is less than 3/2, it is the mean field framework, which is valid. In the intermediate range of $3/2 \leq \sigma \leq 2$ the FM behavior belongs to varied classes such as (3D Ising and tricritical mean field model) which depend on σ.

4. Conclusion

To sum up, it is worth emphasizing that we have studied the structural, magnetic, magnetocaloric and electrical properties of $La_{0.5}Sm_{0.1}Sr_{0.4}Mn_{0.975}In_{0.025}O_3$ perovskite manganite synthesized by sol–gel method. The experimental results have revealed that our sample crystallizes in a single phase with rhombohedral structure ($R\bar{3}c$ space group). A comprehensive and detailed critical behavior study of the ferromagnetic to paramagnetic transition in our manganite has been carried out using magnetic techniques in order to independently extract
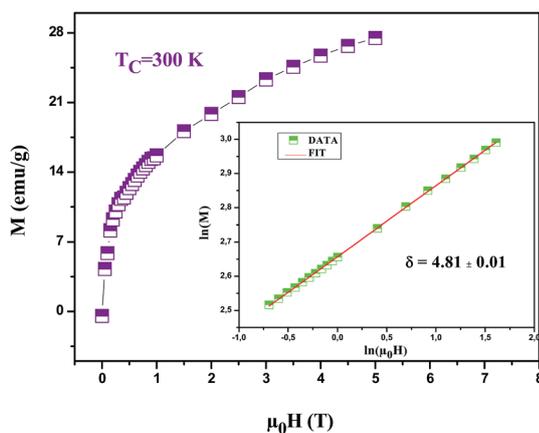
Fig. 10 Isothermal M vs. μ_0H plot of LSSMIO sample at $T_C = 300$ K; the inset shows the same plot in log–log scale and the solid line (red color) is the linear fit following eqn (19).

the critical exponents' β, γ, and δ. The results showed that the 3D Ising model is satisfied, indicating short range-interactions. On the other hand, the resistivity was fitted using the mathematical model (Gauss function). Besides, the resistivity of $La_{0.5}Sm_{0.1}Sr_{0.4}Mn_{0.975}In_{0.025}O_3$ was fitted well with the Gauss function. As far as, we have obtained a promising agreement between the theoretical and the experimental values of T_{M-Sc} and ρ_{max}. The magnetoresistance studies reveal that a high magnetic field has been found to affect MR at T_C. For $\mu_0H = 5$ T, the maximum magnetic entropy change ($-\Delta S_M^{max}$) of 5.25 J kg^{-1} K^{-1} and the relative cooling power (RCP) of 236 J kg^{-1} have been observed near the magnetic transition temperature 300 K. Thus, the broad operating temperature range with moderate values of $-\Delta S_M^{max}$ and RCP make our compound a potential candidate for magnetic refrigeration technology near room temperature.

Conflicts of interest

There are no conflicts to declare.

References

1 Z. Mohamed, E. Tka, J. Dhahri and E. K. Hlil, *J. Alloys Compd.*, 2016, **688**, 1260–1267.
2 R. N. Mahato, K. Sethupathi, V. Sankaranarayanan and R. Nirmala, *J. Appl. Phys.*, 2010, **107**, 09A943.
3 A. M. Tishin and Y. I. Spichkin, *The Magnetocaloric Effect and its Applications*, IOP, Bristol and Philadelphia, 2003.
4 G. Mohamed Amara, Ah. Dhahri, J. Dhahri and E. K. Hlil, *RSC Adv.*, 2017, **7**, 10928.
5 A. Zaidi, T. Alharbi, J. Dhahri, S. Alzobaidi, M. A. Zaidi and E. K. Hlil, *Appl. Phys. A*, 2017, **123**, 94.
6 U. L. Shinde, L. N. Singh and N. B. Srivastava, *Phys. B*, 2014, **452**, 13.
7 C. Zener, *Phys. Rev.*, 1951, **82**, 403.
8 H. E. Stanley, *Introduction to Phase Transitions and Critical Phenomena*, Oxford University Press, London, 1971.
9 M. Seeger, S. N. Kaul, H. Kronmüller and R. Reisser, *Phys. Rev. B: Condens. Matter Mater. Phys.*, 1995, **51**, 12585.
10 Y. Motome and N. Furukawa, *J. Phys. Soc. Jpn.*, 2001, **70**, 1487.
11 Y. Motome and N. Furukawa, *J. Phys. Soc. Jpn.*, 2000, **69**, 3785.
12 K. Ghosh, C. J. Lobb, R. L. Greene, S. G. Karabashev, D. A. Shulyatev, A. A. Arsenov and Y. Mukovskii, *Phys. Rev. Lett.*, 1998, **81**, 4740.
13 Ch. V. Mohan, M. Seeger, H. Kronmuller, P. Murugaraj and J. Maier, *J. Magn. Magn. Mater.*, 1998, **183**, 348.
14 H. S. Shin, J. E. Lee, Y. S. Nam, H. L. Ju and C. W. Park, *Solid State Commun.*, 2001, **118**, 377.
15 H. M. Rietveld, *J. Appl. Crystallogr.*, 1969, **2**, 65.
16 V. M. Goldshmidt, *Geochmische Verteilungsgesetze der Elemente*, 1927–28, vol. VII–VIII.
17 G. Caglioti, A. Paoletti and F. P. Ricci, *Nucl. Instrum. Methods*, 1960, **9**, 195–198.
18 J. Gutiérrez, A. Peña, J. M. Barandiáran, J. L. Pizarro, T. Hernández, L. Lezama, M. Insausti and T. Rojo, *Phys. B*, 2000, **61**, 9028–9035.
19 L. V. Bau, N. V. Khiem, N. X. Phuc, L. V. Hong, D. N. H. Nam and P. Nordblad, *J. Magn. Magn. Mater.*, 2010, **322**, 753.
20 H. S. Shin, J. E. Lee, Y. S. Nam, H. L. Ju and C. W. Park, *Solid State Commun.*, 2001, **118**, 377.
21 G. G. Lonzarich and L. Taillefer, *J. Phys. C: Solid State Phys.*, 1985, **18**, 4339.
22 E. Della Torre, L. H. Bennett and R. E. Watson, *Phys. Rev. Lett.*, 2005, **94**, 147210.
23 C. Bogdan Jurca, Synthèse et caractérisation de pérovskites doubles magnétorésistives dérivées de Sr_2FeMoO_6, PhD thesis, Université Paris Sud, Paris XI, 2004.
24 S. de Brion, F. Ciorcas, G. Chouteau, P. Lejay, P. Radaelli and C. Chaillout, *Phys. Rev.*, 1999, **B59**, 1304.
25 W. F. Giauque and D. P. McDougall, *Phys. Rev.*, 1933, **43**, 768.
26 H. Ishimoto, N. Nishida, T. Furubayashi, M. Shinohara, Y. Takano, Y. Miura and K. Ono, *J. Low Temp. Phys.*, 1984, **55**, 17.
27 Z. Mohamed, M. Abassi, E. Tka, J. Dhahri and E. K. Hlil, *J. Alloy. Compd.*, 2015, **646**, 23–31.
28 K. A. Gschneidner Jr, V. K. Pecharsky and A. O. Tsokol, *Rep. Prog. Phys.*, 2005, **68**, 1479.
29 A. Dhahri, J. Dhahri, E. K. Hlil and E. Dhahri, *J. Alloys Compd.*, 2012, **530**, 1.
30 S. Mnefgui, A. Dhahri, N. Dhahri, E. K. Hlil and J. Dhahri, *J. Magn. Magn. Mater.*, 2013, **340**, 91.
31 V. K. Pecharsky, K. A. Gschneidner and A. O. Tsokol, *Rep. Prog. Phys.*, 2005, **68**, 1479.
32 D. T. Morelli, A. M. Mance, J. V. Mantese and A. L. Micheli, *J. Appl. Phys.*, 1996, **79**, 373.
33 M. Foldeaki, R. Chahine and T. K. Bose, *J. Appl. Phys.*, 1995, **77**, 3528.
34 H. Yang, Y. H. Zhu, T. Xian and J. L. Jiang, *J. Alloys Compd.*, 2013, **555**, 150.
35 X. X. Zhang, G. H. Wen, F. W. Wang, W. H. Wang, C. H. Yu, et al., *Appl. Phys. Lett.*, 2000, **77**, 3072.
36 M. Abassi, N. Dhahri, J. Dhahri and E. K. Hlil, *Phys. B*, 2014, **449**, 138–143.
37 Y. Sun, W. Tong and Y. Zhang, *J. Magn. Magn. Mater.*, 2001, **232**, 205–208.
38 K. Dhahri, N. Dhahri, J. Dhahri, K. Taibi, E. K. Hlil, H. Belmabroukd and M. Zaidi, *RSC Adv.*, 2017, **7**, 43410.
39 Q. Y. Dong, H. W. Zhang, J. R. Sun, B. G. Shen and V. Franco, *J. Appl. Phys.*, 2008, **103**, 116101.
40 L. Changshi, *J. Chem. Eng. Data*, 2011, **56**, 2.
41 G. Venkataiah, V. Prasad and P. V. Reddy, *J. Alloys Compd.*, 2007, **429**, 1–9.
42 D. S. Rana, K. R. Mavani, C. M. Thaker, D. G. Kuberkar, C. D. Kundaliya and S. K. Malik, *J. Magn. Magn. Mater.*, 2004, **271**, 215–223.
43 S. Rößler, U. K. Rößler, K. Nenkov, D. Eckert, S. M. Yusuf, K. Dörr and K.-H. Mülle, *Phys. Rev. B: Condens. Matter Mater. Phys.*, 2004, **70**, 104417.
44 A. Arrot and J. E. Noakes, *Phys. Rev. Lett.*, 1967, **19**, 786.
45 B. Widom, *J. Chem. Phys.*, 1965, **43**, 3898.

46 S. K. Banerjee, *Phys. Lett.*, 1964, **12**, 16.

47 J. S. Kouvel and M. E. Fisher, *Phys. Rev.*, 1964, **136**, A1626.

48 H. S. Shin, J. E. Lee, Y. S. Nam, H. L. Ju and C. W. Park, *Solid State Commun.*, 2001, **118**, 377.

49 S. N. Kaul, *J. Magn. Magn. Mater.*, 1985, **53**, 5.

50 M. Pękała, *J. Appl. Phys.*, 2010, **108**, 113913.

51 W. Chen, L. Y. Nie, W. Zhong, Y. J. Shi, J. J. Hu, A. J. Li and Y. W. Du, *J. Alloy. Compd.*, 2005, **395**, 23–25.

52 Z. B. Guo, Y. W. Du, J. S. Zhu, H. Huang, W. P. Ding and D. Feng, *Phys. Rev. Lett.*, 1997, **78**, 1142.

53 M. Nasri, M. Triki, E. Dhahri and E. K. Hlil, *J. Alloys Compd.*, 2013, **546**, 84–91.

54 S. Mnefgui, A. Dhahri, N. Dhahri, E. K. Hlil and J. Dhahri, *Solid State Sci.*, 2013, **21**, 19.

55 T.-L. Phan, Y. D. Zhang, P. Zhang, T. D. Thanh and S. C. Yu, *J. Appl. Phys.*, 2012, **112**, 093906.

56 D. Kim, B. L. Zink, F. Hellman and J. M. D. Coey, *Phys. Rev. B: Condens. Matter Mater. Phys.*, 2002, **65**, 214424.

57 T. D. Thanh, D. C. Linh, T. V. Manh, T. A. Ho, T.-L. Phan and S. C. Yu, *J. Appl. Phys.*, 2015, **117**, 17C101.

58 M. Dhahri, J. Dhahri and E. K. Hlil, *J. Magn. Magn. Mater.*, 2017, **434**, 100–104.

59 M. E. Fisher, S.-K. Ma and B. G. Nickel, *Phys. Rev. Lett.*, 1972, **29**, 917–920.